Title: Acceleration of a large deep-seated tropical landslide due to urbanisation feedbacks

Author list:

Antoine Dille[1,2*+], Olivier Dewitte[1], Alexander Handwerger[3,4], Nicolas d'Oreye[5,6], Dominique Derauw[5,7,8], Gloire Ganza Bamulezi[9,10], Guy Ilombe Mawe[9,11], Caroline Michellier[1], Jan Moeyersons[1], Elise Monsieurs[1], Toussaint Mugaruka Bibentyo[1,9,12], Sergey Samsonov[13], Benoît Smets[1,2], Matthieu Kervyn[2], François Kervyn[1]

Affiliations:

[1] *Department of Earth Sciences, Royal Museum for Central Africa, Tervuren, Belgium*
[2] *Department of Geography, Vrije Universiteit Brussel, Brussels, Belgium*
[3] *Joint Institute for Regional Earth System Science and Engineering, University of California, Los Angeles, CA, USA*
[4] *Jet Propulsion Laboratory, California Institute of Technology, Pasadena, CA, USA*
[5] *European Centre for Geodynamics and Seismology, Walferdange, Luxembourg*
[6] *National Museum of Natural History, Luxembourg, Luxembourg*
[7] *Instituto de Investigación en Paleobiología y Geología, Universidad Nacional de Rio Negro - CONICET, Río Negro, Argentina*
[8] *Centre Spatial de Liège, Université de Liège, Angleur, Belgium*
[9] *Département de Géologie, Université Officielle de Bukavu, Bukavu,*
[10] *Département de Géologie, Service Géologique National du Congo, Kinshasa, DR Congo*
[11] *Department of Geography, University of Liège, Liège, Belgium*
[12] *Department of Geology, Ghent University, Ghent, Belgium*
[13] *Canada Centre for Mapping and Earth Observation, Natural Resources Canada, Ottawa, Canada*

*Corresponding author: antoine.dille@gmail.com
[+]Present affiliation: Royal Belgian Institute of Natural Sciences, Operational Directorate Natural Environments, Brussels, Belgium

KEYWORDS: landslide controls, rainfall infiltration, urbanisation, ground deformation, InSAR, historical aerial photographs, Africa

Abstract

The movement of large, slow-moving deep-seated landslides is principally regulated by changes in pore-water pressure in the slope. In urban areas, drastic reorganisation of the surface and subsurface hydrology – e.g., associated with roads, housings, or storm drainage – may alter the latter, and ultimately the slope stability. Yet, our understanding of the influence of slope urbanisation on the dynamics of landslides remains elusive. Here we combined satellite and (historical) aerial images to quantify how 70 years of hillslope urbanisation changed the seasonal, annual and multi-decadal dynamics of a large slow-moving landslide located in the tropical environment of the city of Bukavu, Democratic Republic of the Congo. Analysis of week-to-week landslide motion over the past 4.5 years reveals that it is closely tied to pore-water pressure changes, pointing to interacting influences from climate, weathering, tectonics and urban development on the landslide dynamics. Over decadal timescales, we find that the sprawl of urbanised areas led to the acceleration of a large section of the landslide, which was likely driven by self-reinforcing feedbacks involving slope movement, rerouting of surface water flows, and pipe ruptures. As hillslopes in many tropical cities are being urbanised at an accelerating pace, better understanding how anthropogenic activity influences surface processes will be vital to effective risk planning and mitigation.

Main text:

The current rate and scale of urban growth are unprecedented in human history[1,2]. This urban transition is mostly occurring in Africa and Asia, where largely young urban landscapes expand in an informal and expansive manner[1,2]. This sprawl often overlooks natural constraints from the environment – therefore drastically increasing the population exposed to natural hazards[3,4]. On urbanised hillslopes, dozens of lives are claimed annually by shallow high-velocity landslides[4–7], whereas deeper, slow, but continuously moving landslides act as a more pervasive hazard and lead to the progressive destruction of infrastructures and housings[5,8–10]. How such slow-moving, deep-seated landslides respond to natural stress perturbations (e.g., seasonal[11–13] or multi-annual precipitations[14,15], seismic disturbance[16,17], undrained loading[18] or even atmospheric pressure changes[19]) has long been studied in natural environments; simplified mechanisms showing that rainfall-induced changes in pore-water pressure are principally regulating their motion[9,11–13,20–22]. Yet, while hydrologists have long

recognized that urbanisation has dramatic impacts on catchment hydrology[23–25], very little is known on the influence of urbanisation on landslide motion patterns. Quantifying how progressive hillslope urbanisation changes the dynamics of deep slow-moving landslides is one of our research objectives. To this end, we study the seasonal, annual and multi-decadal dynamics of a large slow-moving landslide located in the rapidly expanding city of Bukavu in eastern DR Congo.

Seen as a safe haven in a region where violent conflicts have forced thousands to move over the last decades, Bukavu is exemplative of those cities facing rapid and informal growth[26–28]. Originally established along the flat shoreline of the southern tip of Lake Kivu (Bukavu micro-graben[29]), the city progressively expanded on the steep slopes of the Kivu Rift[26] (Fig. 1a,b, Extended Data Fig. 1). Sited in a tropical and tectonically active landscape – where environmental conditions (climate, weathering, lithology, tectonics) are generally particularly favourable to slope failures[30,31] – about one-third of the city is today built on large deep-seated landslides[32]. Most are dormant (or relict) slope failures, but portions of the city are affected by slow and continuous destruction of infrastructures and housings due to ground surface motion. One of these zones is the Funu neighbourhood. Hosting today more than 80,000 inhabitants living in overcrowded, poor-quality housing with inadequate infrastructure[26], Funu neighbourhood is built on a single, slow but continuously moving landslide (Fig. 1bcde). Developed in deeply weathered tertiary and quaternary basaltic lava layers[29], this large landslide – estimated volume of ca. 60 ± 30 x 10^6 m^3, area of 1.6 km^2 and shear surface depth estimated to vary from 30 to 80 m – is of probable seismo-tectonic origin[29] and clearly precedes human activity in the area[32]. Here we present a long-term analysis of the dynamics of Funu landslide from its pre-urbanisation conditions (first archives date from 1947) until today's mostly informal and extremely dense occupation. The historical, political, and socio-economic context of the country – and of this region in particular[26] – have an immediate impact on availability of past knowledge and impose challenges on data collection. Therefore, we rely primarily on state-of-the-art remote sensing to apprehend constraints on deep-seated landslide processes imposed by tropical[30,31] and urban environments[33].

[Fig. 1. | Landslides in the city of Bukavu.]

Landslide structure and seasonal controls

We use satellite radar interferometry (InSAR) to quantify landslide motion for the period 2015-2019 (Fig. 2abc; Fig. 3; Extended Data Fig. 2). Using the Multidimensional Small Baseline Subset (MSBAS) method[35,36], we combine 2,575 ascending and descending interferograms from both Sentinel-1 and COSMO-SkyMed (CSK) sensors to measure 2D and 3D surface motion with a sub-weekly temporal resolution (see Methods). Max InSAR velocities over the landslide are 0.1 m yr^{-1} towards the east, 0.08 m yr^{-1} southwards and 0.05 m yr^{-1} vertically downwards. We also apply automated pixel tracking on Pléiades and Unoccupied Aircraft System (UAS) orthomosaics to measure surface displacements too large to be captured by conventional InSAR[22,36,37] (see Methods). It provides velocity estimates for a relatively fast-moving 0.14-km^2 zone (latter referred to as 'fastest unit') that has average and max horizontal surface velocity of 0.6 m yr^{-1} and 3 m yr^{-1} (measured for both 2013-2018 and 2017-2018 periods; Fig. 2d). Strains rates (Fig. 2e) indicate zones of stretching, shearing and shortening at the landslide surface, dominated by the deformation signal over this fastest portion of the landslide. Strong deformation gradients explain the magnitude of damages to infrastructures and housings[38] (Extended Data Fig. 3). Patterns of surface deformation and strain illustrate discontinuities and the presence of multiple morphologic and kinematic units (Extended Data Figs. 4,5). Common in large landslide complexes, these zones reflect spatial heterogeneity in conditions controlling landslide movement (e.g., bedrock geometry, hydrological material properties, weathering[39,40]).

[Fig. 2. | Landslide motion and surface strains.]

We use the InSAR time series to constrain the seasonal and annual dynamics of individual landslide units, sorted in three groups depending on their kinematic behaviour (see Methods, Fig. 3 and Extended Data Figs. 5,6,7). Funu landslide moves near continuously over the year, without month(s)-long halt during the dry season[15,17] and there is no apparent minimum rainfall required to trigger landslide motion, such as observed for many landslides formed in clay-rich lithologies[41]. We find close feedbacks between changes in simulated pore-water pressure (modelled using a simple 1D hydrological model[13,15], see Methods) and landslide kinematics, that is consistent over the 4.5 years covered by our dataset (Fig. 3abc). For all landslide units, lowest velocities are measured at the end of the dry season (September) and

rise very rapidly (average time lag is 12 days, see Supplementary Fig. 1) following increase in simulated pore-water pressure associated with the onset of the wet season. The landslide reaches its velocity maxima at the end October or December depending on the location within the landslide (Fig. 3, Extended Data Fig. 7). After a temporary decrease in velocity during the relatively drier months of January and February, a second velocity peak is observed around May (the last month of the wet season) or June-July (middle of the dry season) depending on the landslide unit, before velocities hit their minima at the end of the dry season (see Supplementary Discussion). We also explore the influence of nearby medium-intensity earthquakes (Mw 4.7 – 5.8) on the landslide kinematics. We find no clear relation between the timing of nearby medium-intensity earthquakes (Mw 4.7 – 5.8) and changes in landslide motion. While the highest landslide velocities in our study period occurred following the August 2015 Mw 5.8 earthquake, the 2016 wet season was also the wettest (1480 mm) over the observation period. More work is needed to better understand the combined role of earthquakes and precipitation, which have been shown to work together to promote instability of slow-moving landslides[17]. Following the 2016 wet season, we observe an overall decrease in landslide velocities (see Extended Data Fig. 6).

[Fig. 3. | Landslide displacement, pore pressure and rainfall times series.]

The feedbacks between landslide velocity, rainfall, and simulated pore-water pressure indicate that near-surface groundwater flow plays a key role in the week-to-week landslide kinematics, with increased rainfall (and related increase in pore-water pressure) resulting in low effective stress (defined as normal stress minus pore-water pressure) in the slope that promotes landslide motion[11,12]. Interestingly, rapid acceleration of the landslide occurs both at the onset of the wet season (when groundwater table is expected to be at its lowest) and with more intense rainy days during the wet season (when groundwater table level is expected to be high). These changes in landslide kinematics suggest that minor changes in effective stress control changes in velocity[42], with the landslide remaining close to an acceleration threshold[11,12] all year long. This observation is consistent with the landslide "bathtub hypothesis", where landslides remain wet year-round because low-permeability shear zones prevent groundwater drainage and hydrologically isolate landslides from their surroundings[13,43].

While most studies focusing on the kinematics of deep-seated landslides showed that prolonged periods of increased precipitation were necessary to trigger acceleration at the onset of the wet season[11–13,44,45], the rapid response of Funu landslide to rainfall is surprising; notably given its large inferred depth (~30-80 m; response time is predicted to scale with depth). Such behaviour is however not unique[44,46], and our very-high InSAR sampling frequency may also capture a response that is usually missed with lower sampling frequency conventional InSAR or satellite optical measurements. Yet, many environmental factors – tropical climate, weathering, tectonic settings and urban development – are acting on Funu hydrology and may each influence its relatively singular kinematic response. While preferential infiltration pathways are commonly believed to play a key role in explaining rapid landslide responses[39,46,47], intense rainfall associated with tropical climate[30] may exacerbate their relative importance. Slope mechanical and hydrological properties are also known to be strongly influenced by weathering process[31,48,49], a central component of tropical geomorphology[30]. The basaltic layers in which Funu landslide developed are a good illustration: a succession of deeply weathered quaternary and tertiary lava layers[29] with springs at various elevations (Fig. 4a) attesting both of a modified permeability and a heterogenous alteration between landslide units. Weathering-related weakening of the slope mechanical properties and preferential infiltration pathways are probably further promoted by faulting and the long-lasting influence of recurrent seismicity[17,50]. All these natural constraints are commonly recognised for influencing the stability of (tropical) slopes[30,47], and we can reliably assume they act on the dynamics of Funu landslide.

The landslide can however not be defined through its natural context alone. Natural lands were converted to urban lands (see Fig. 1, Extended Data Fig. 3), profoundly modifying how and where water infiltrates (e.g., due to impervious surfaces, soil compaction, drainage systems, etc.) as well as the sources and locations of slope recharge (e.g., additional water carried from other catchments, blockages and leaks from drainage, distribution and septic systems; Fig. 4, Extended Data Fig. 8)[6,23,24]. These drastic and extensive reorganisations of surface and subsurface water pathways[24], leads to changes in the distribution of water within the slope, so that diffuse infiltration is largely replaced by forced point infiltration of unproportionally high water volumes on places where they do not belong naturally[6,48,51].

Altogether, urbanisation results in large-scale modifications of slope groundwater[23–25], and this in turn directly affects the hillslope stress state[6,33,51,52].

[Fig. 4. | Surface drainage.]

We find that seasonal rainfall is the principal regulator of weekly to yearly motion of the Funu landslide. However, the infiltrating rainfall and groundwater is impacted by the local environment, including the tropical climate, rock type, tectonics, and urban landscape that all influence the slope hydrological conditions and the slope stress state. The individual roles of these parameters are difficult to disentangle over the 4.5-year period captured by InSAR and optical imagery. Yet, by looking at landslide changes over decadal timescales, which better captures the timescales of urban development, we can directly explore the influence of urbanisation on the landslide behaviour.

70 years of hillslope changes

To explore the impact of urbanisation on tropical landslides, we analyse the multi-decadal dynamics of the Funu landslide from the earliest stages of hillslope urbanisation. Urban growth (period 1947-2018) and surface motion (period 1959-2018) are quantified using historical aerial photos and very-high resolution satellite imagery (see Methods, Fig. 5 and Extended Data Figs. 9, 10). Funu landslide was progressively urbanised from its toe to its head. Located higher up in the slope, the 'fastest unit' was thus urbanised later than the 'central units' and 'active toe' – notably in the '90s and early '00s when violent conflicts and insecurity in the region drove important rural-urban migration[26–28]. All three units were moving at the same pace during the earliest stage of urbanisation. While surface velocities remain relatively stable over time for both 'central units' and 'active toe', we observe an acceleration of the 'fastest unit' from the 1974-2001 period onwards. Its timing coincides with an intensification of the urbanisation of the unit, but no such effect was observed for 'central units' nor 'active toe' (Fig. 5). The urban fabric being roughly similar over the entire landslide – dominated by light, one to two-story wooden structures[26,38] – and the acceleration occurring while the 'fastest unit' was only half urbanised; we hypothesize that the acceleration is the consequence of a change to the slope hydrology rather than e.g., a change due to increased loading from infrastructures (Supplementary Discussion). The rerouting of surface and subsurface water – associated with the construction of roads, housings, storm drainage and other infrastructures[23–25] – concerns all landslide units. Unlike the other two, however, the

219 'fastest unit' lies at the convergence of slope drainage systems. The concentration of
220 additional water from the establishment of new water flow paths – also conveying water from
221 outside the natural catchment (Fig. 4ab, Extended Data Fig. 8) – and leaks from inadequate,
222 blocked or damaged sewage and storm drains (Fig. 4cde) therefore added extra water to
223 zones already closer to saturation conditions and naturally nearby to a tipping point. The
224 destabilisation of the 'fastest unit' further caused a series of self-reinforcing feedbacks:
225 motion favouring leaks and pipe ruptures[38], which locally promoted saturation conditions and
226 instability. In this context we also observe the development of deep gullies alongside the
227 lateral margins of the 'fastest unit'[38] (Fig. 4c, Extended Data Fig. 9). These gullies now favour
228 both a stabilisation (with the lowering of the water table) and a destabilisation (due to
229 debutressing) of the unit, the latter most likely playing the leading role (Supplementary
230 Discussion). The analysis of the current landslide kinematics demonstrated how minor
231 changes in effective stress control changes in velocity, providing essential keys to
232 comprehend how (relatively) subtle modifications at the landslide surface may have affected
233 the overall landslide behaviour. Further, the timing and spatial scale of the destabilisation –
234 that affects only the 'fastest unit' and not the adjacent slopes – supports the role of local-
235 scale surface and near-surface changes associated with urbanisation rather than regional-
236 scale changes associated with seismicity and/or rainfall; i.e. the two key regional drivers that
237 could be invoked for altering the stability conditions of the hillslope. Besides, neither changes
238 in seismic patterns nor in rainfall patterns are demonstrated in the last decades in the region;
239 yet with relatively low confidence due to limited evidence[53–55].

240 **[Fig. 5. | Urban growth and slope instability from 1947 to 2018.]**

241 **Implications for landslide hazard and mitigation strategies**

242 Our findings show that urbanisation can interfere with the natural behaviour of long-lived,
243 deep-seated landslides. Such relationship is not surprising given how urbanisation is known
244 to affect slope hydrology[23–25] and how slope hydrology in turn regulates the motion of most
245 slow-moving landslides[9,11–13,20–22]. Large slow-moving landslides are known to sometimes
246 abruptly transition from slow motion to catastrophic failure[15,56]. Concerns are obviously
247 higher when the landslide is embedded in a dense urban landscape. Avoidance of unstable
248 slopes is usually not an option in developing countries, where informal urbanisation generally
249 outstrips any regulation[57]. Mitigation strategies aiming at reducing water infiltration by a

comprehensive management of all forms of surface water should be backed[58]. Those are complex to implement – especially for such large landslides – and, while landsliding is not the primary concern of the urban population of Bukavu (primary concerns include access to potable water, sanitation, health or education services and (food) security[26]), community-based approaches[52,58] should be promoted to prevent loss of life and infrastructures due to landsliding. As hillslopes of the world's cities are being urbanised at accelerating paces[6,7], we believe that more studies are needed to improve our understanding of how anthropogenic activity influences surface processes and landscape evolution. This would ensure the valid evaluation of landslide hazard and optimisation of mitigation strategies.

Acknowledgements

This article is a contribution in the framework of the projects RESIST funded by the Belgian Science Policy (BELSPO), Belgium (SR/00/305) and the Fonds National de la Recherche, Luxembourg (INTER/STEREOIII/13/05/RESIST/d'Oreye); MODUS (SR/00/358), AfReSlide (BR/121/A2/AfReSlide) and PAStECA (BR/165/A3/PASTECA) research projects funded by BELSPO and RA_S1_RGL_GEORISK and HARISSA funded by Development Cooperation programme of the Royal Museum for Central Africa that is supported directly by the Directorate-General Development Cooperation and Humanitarian Aid of Belgium. Elise Monsieurs benefited from a F.R.S. – FNRS PhD scholarship. Part of this research was performed at the Jet Propulsion Laboratory, California Institute of Technology, under a contract with the National Aeronautics and Space Administration (80NM0018D0004). COSMO-SkyMed images were acquired through RESIST and MODUS projects as well as the CEOS Landslide Pilot. The images are under an Italian Space Agency (ASI) licence. Part of this research was performed at the Jet Propulsion Laboratory, California Institute of Technology under contract with NASA. Special thanks go to Université Officielle de Bukavu, and particularly to the members of the Department of Geology. Together with the support of the Civil Protection of South Kivu, they made possible to execute fieldwork in the study area, provided crucial help for the dGNSS acquisition campaigns and the many discussions on landslide processes in the area. We thank Damien Delvaux for sharing field pictures and discussions on the tectonic and geology of the area. We further wish to thank Georgina Bennett, Pablo Gonzalez, Jean-Philippe Malet and Martin

Rutzinger for their insightful discussions and recommendation regarding this research as well as three reviewers whose comments helped improving this manuscript.

Author contribution statement

A.D. and O.D. conceived the study with inputs from F.K. and M.K.. A.D. processed and analysed the data and created the figures. A.D. wrote the manuscript, with main inputs from O.D. and key contribution from M.K. and A.H.. A.D., O.D., F.K., G.B.G., G.I.M., E.M. and T.M.B. participated in the field data acquisition and interpretation. C.M. and J.M. participated in the interpretation of the field data. N.dO., D.D., S.S. and B.S. assisted the processing of SAR and UAS data. A.H. assisted the processing of slope pore-water simulations. All the authors contributed to the final version of the paper. O.D. and F.K. coordinated and designed this collaborative study in the frame of the RESIST and MODUS projects.

Competing interest statement**:**

The authors declare no competing interests.

Figures:

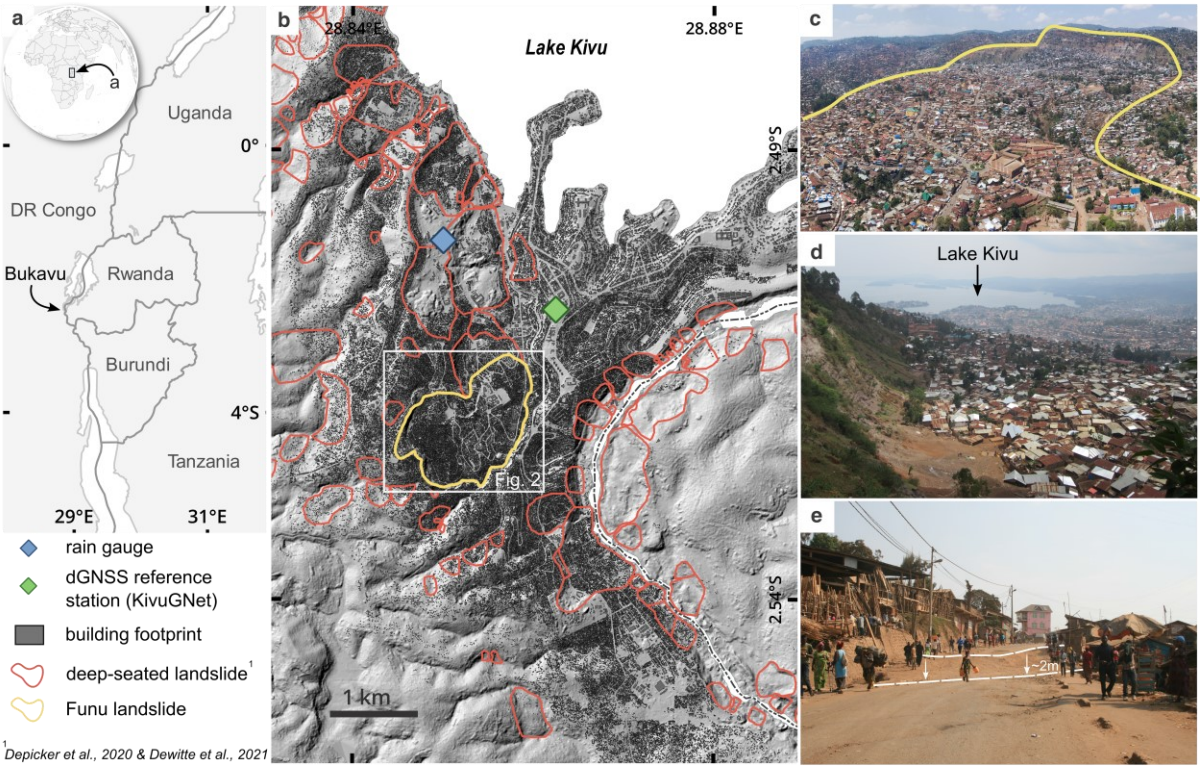

Fig. 1. | Landslides in the city of Bukavu. a, Location of Bukavu, DR Congo. **b**, Outlines of Funu landslide (in yellow) and other deep-seated landslides[32,34] (in red) mapped in the area. The footprint of individual buildings is shown in black (© *Open Street Map* contributors). Background digital elevation model is obtained from photogrammetric processing of stereo Pléiades images from July 2013 (see Methods). **c**, UAS image of Funu landslide (Oct. 2018). **d**, View of the landslide headscarp; Lake Kivu is visible in the background. **e**, Meter-scale gap in the road illustrating the damages to infrastructures caused by continuous landslide movements.

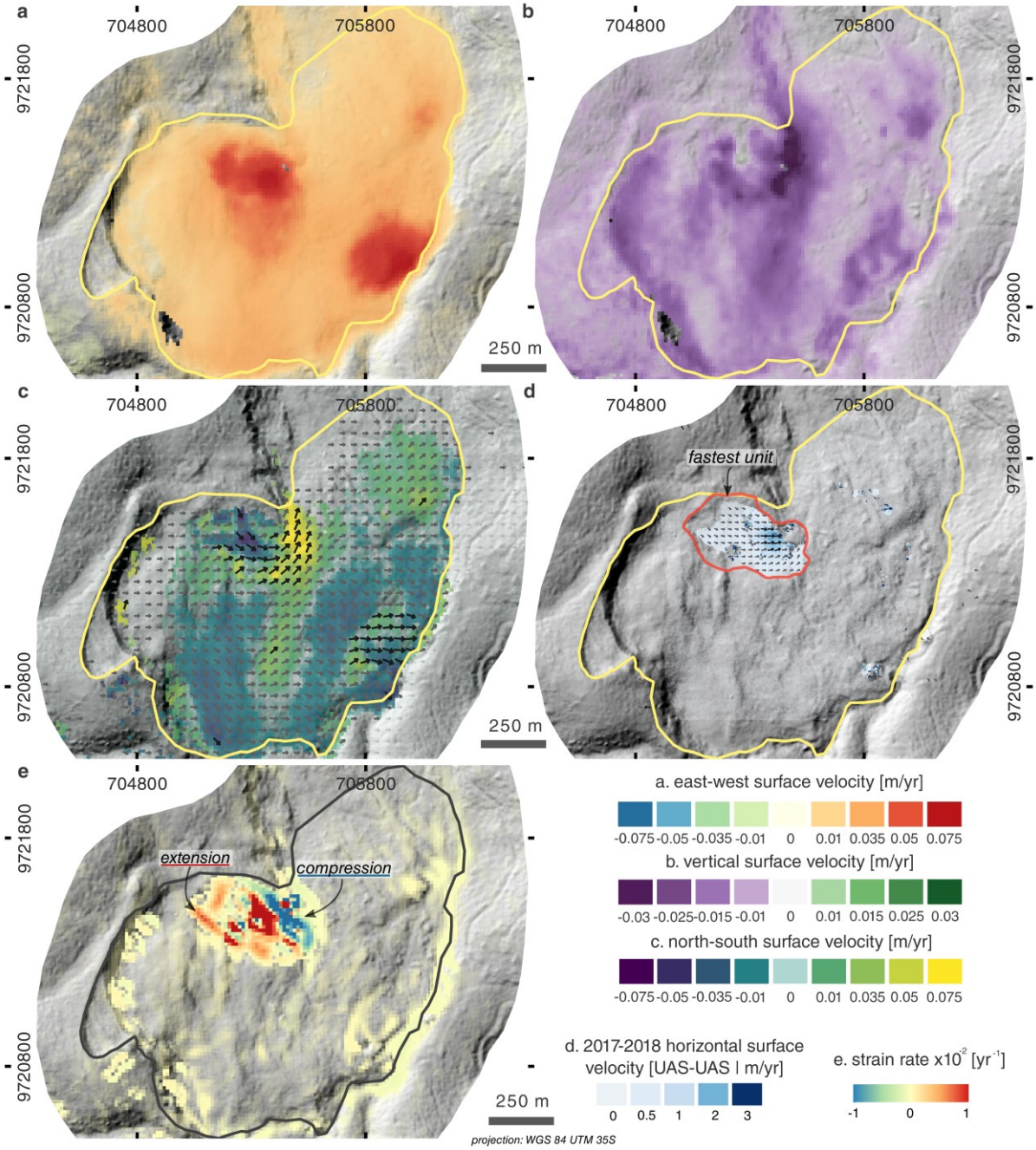

Fig. 2. | Landslide motion and surface strains. a, East-west, **b**, vertical and **c**, north-south surface velocities measured from the combined interferometric processing of CSK and Sentinel-1 images (March 2015 - August 2019). Arrows in **c**, illustrate the direction of surface motion from 3D InSAR. **d**, Horizontal surface velocities measured from automated pixel tracking applied to UAS-SfM orthomosaics (Oct. 2017 – Oct. 2018). **e**, Strain rates measured from combining velocity fields from SAR interferometry and automated pixel tracking. Background digital elevation model is obtained from photogrammetric processing of stereo Pléiades images from July 2013 (see Methods).

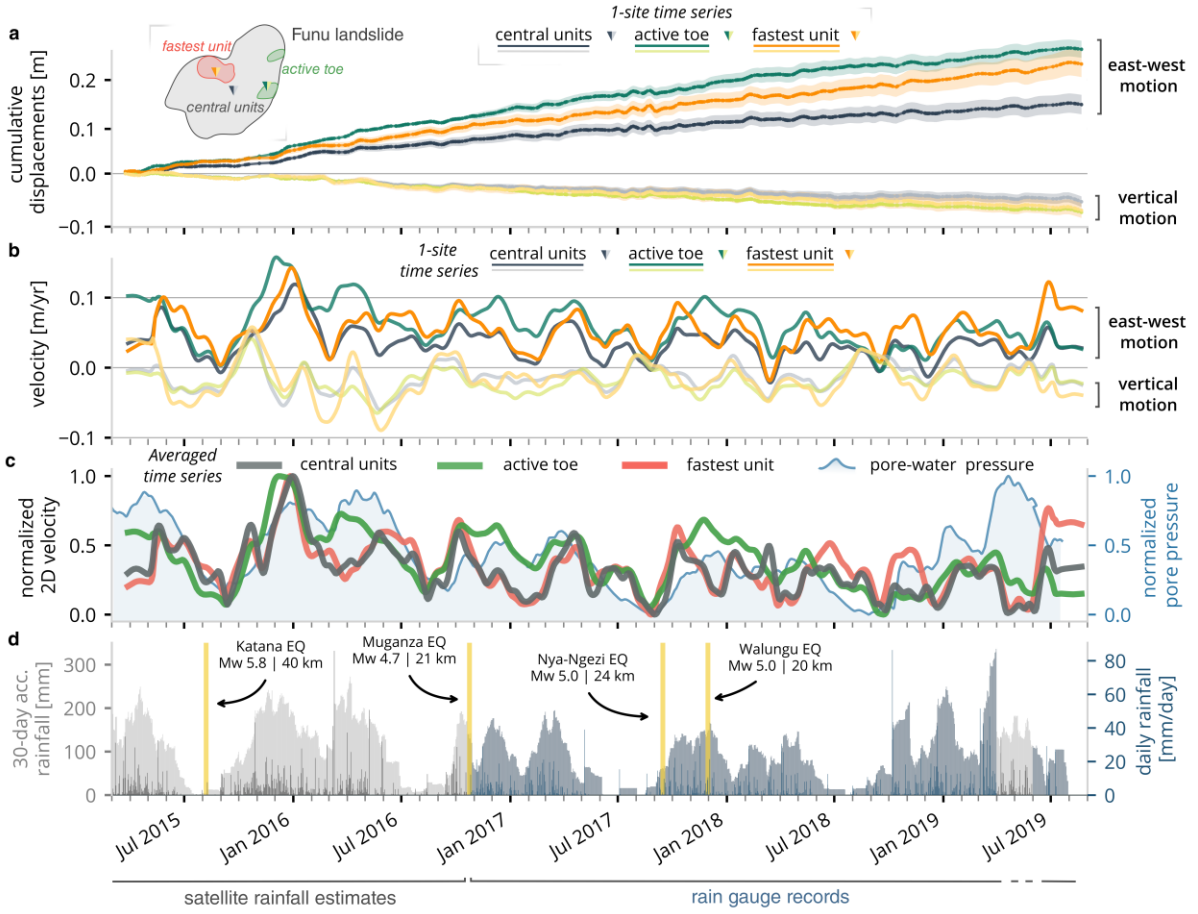

Fig. 3. | Landslide displacement, pore pressure and rainfall times series. a, East-west and vertical cumulative displacements measured by SAR interferometry for three individual sites within the landslide (located by a triangle in subset). Uncertainties are estimated for each site from the standard deviation of the displacement measured over the four neighbouring pixels. **b**, East-west and vertical velocity time series for the same locations. **c**, Average 2D velocity time series over 3 different kinematic units. Time series for 'central units' shows mean velocity from 11 individual sites, 'active toe' from 3 sites and the 'fastest unit' 7 sites (see Extended Data Fig. 5). Changes in velocity are compared to rainfall-induced changes in pore-water pressure simulated through a simple, homogenous 1D diffusion model. Values are normalized to range between minimum (min = 0) and maximum (max = 1). **d**, Earthquake (Mw ≥4.7) and rainfall time series for Bukavu. Rainfall data consists of rain gauge measurements acquired ~2km from the landslide for October 2016 – April 2019, completed by satellite rainfall estimates (IMERG-GPM v6) over the period 2000 – 2019. 30-day accumulation (dark grey/blue shades) and daily rain amounts (dark grey/blue bars) are represented.

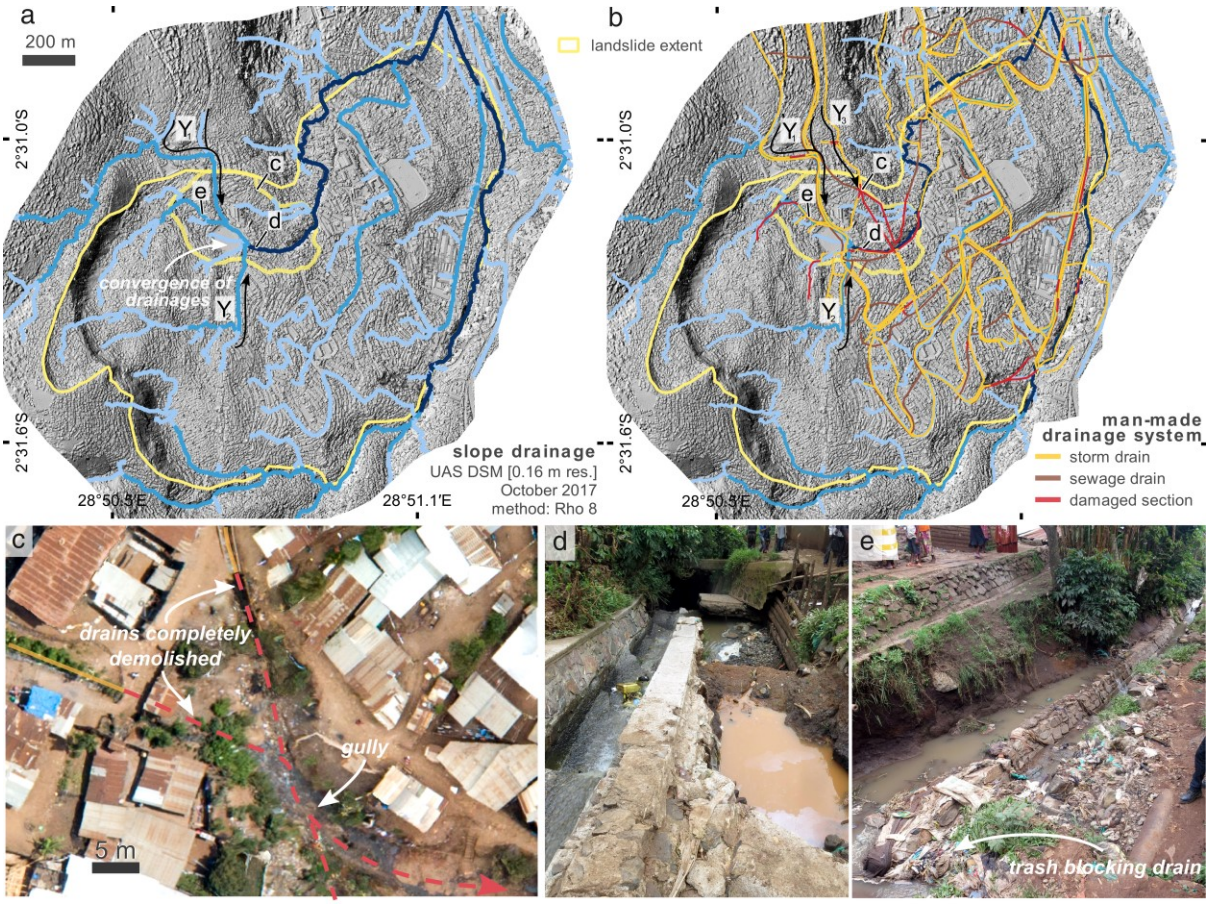

332

333 **Fig. 4. | Surface drainage. a**, Slope and **b,** man-made (storm and sewage drains)
334 drainage over Funu landslide. Arrows (Y_x) highlight zones outside the natural
335 catchment of the 'fastest unit' from which water is conveyed by roads, housing and
336 storm drainage systems. **c,** Example of drains destroyed by landslide motion at the
337 edge of the 'fastest unit'. **d,e,** represent some of the many places where storm drains
338 are inadequate, damaged and/or blocked by trash (pictures by D. Delvaux, RMCA).

339

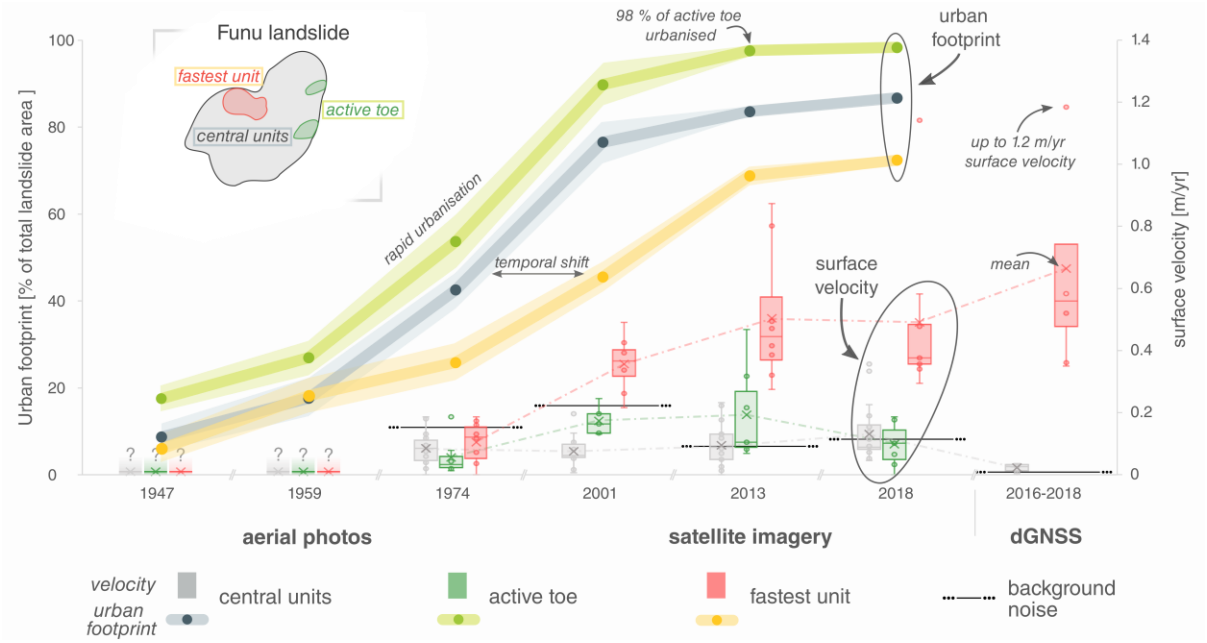

Fig. 5. | Urban growth and slope instability from 1947 to 2018. Historical aerial photos (1947, 1959 and 1974) and satellite imagery (2001, 2013 and 2018) are used to constrain velocity changes and progressive urbanisation of Funu landslide (images shown in Extended Data Fig. 9). Landslide velocity and urbanisation is estimated for the three kinematic units (i.e., 'central units', 'fastest unit' and 'active toe'). Surface velocity for e.g., 1974 shows average over the landslide unit for the period 1959 - 1974. Urbanisation being limited to the toe of the landslide in 1947, surface velocities could not be estimated for the period 1947-1959. Boxes and whiskers show the distribution of velocities measured in each unit. Box bounds show lower and upper quartiles, while the mean value is expressed as a 'X' and the median as a horizontal bar. 'Background noise' represents the measured average velocity in presumably stable areas outside the landslide – therefore considered as a proxy for noise level. Velocities from dGNSS surveys campaigns over 20 benchmarks are also shown for the period 2016-2018 for central and fastest units.

References

1. Seto, K. C., Fragkias, M., Gu, B. & Reilly, M. K. A Meta-Analysis of Global Urban Land Expansion. *PLoS One* **6**, 9 (2011).

2. Ramalho, C. E. & Hobbs, R. J. Time for a change: Dynamic urban ecology. *Trends Ecol. Evol.* **27**, 179–188 (2012).

3. Pelling, M. *The Vulnerability of Cities: Natural Disasters and Social Resilience*. *Earthscan Publications* (Routledge, 2003).

4. Ozturk, U. *et al. Nature* **608**, 262–265 (2022).

5. Alexander, D. Urban landslides. *Prog. Phys. Geogr.* **13**, 157–189 (1989).

6. Schuster, R. L. & Highland, L. M. The third hans cloos lecture. Urban landslides: Socioeconomic impacts and overview of mitigative strategies. *Bull. Eng. Geol. Environ.* **66**, 1–27 (2007).

7. Larsen, M. C. Rainfall-triggered landslides, anthropogenic hazards, and mitigation strategies. *Adv. Geosci.* **14**, 147–153 (2008).

8. Aleotti, P. & Chowdhury, R. Landslide hazard assessment summary review and new perspectives. *Bull. Eng. Geol. Environ.* **58**, 21–44 (1999).

9. Carey, J. M., Massey, C. I., Lyndsell, B. & Petley, D. N. Displacement mechanisms of slow-moving landslides in response to changes in porewater pressure and dynamic stress. *Earth Surf. Dyn.* **7**, 707–722 (2019).

10. Lacroix, P., Handwerger, A. L. & Bièvre, G. Life and death of slow-moving landslides. *Nat. Rev. Earth Environ.* **1**, 404–419 (2020).

11. Iverson, R. M. & Major, J. J. Rainfall, ground-water flow, and seasonal movement at Minor Creek landslide, northwestern California: physical interpretation of empirical relations. *Geol. Soc. Am. Bull.* **99**, 579–594 (1987).

12. Hilley, G., Bürgmann, R., Ferretti, A., Rocca, F. & Novali, F. Dynamics of Slow-Moving Landslides from Permanent Scatterer Analysis. *Science (80-.).* **304**, 1952–1955 (2004).

13. Handwerger, A. L., Roering, J. J. & Schmidt, D. A. Controls on the seasonal deformation of slow-moving landslides. *Earth Planet. Sci. Lett.* **377**–**378**, 239–247 (2013).

14. Bennett, G. L. *et al.* Historic drought puts the brakes on earthflows in Northern California. *Geophys. Res. Lett.* **43**, 5725–5731 (2016).

15. Handwerger, A. L., Huang, M.-H. H., Fielding, E. J., Booth, A. M. & Bürgmann, R. A shift from drought to extreme rainfall drives a stable landslide to catastrophic failure. *Sci. Rep.* **9**, 1–12 (2019).

16. Lacroix, P., Berthier, E. & Maquerhua, E. T. Earthquake-driven acceleration of slow-moving landslides in the Colca valley, Peru, detected from Pléiades images. *Remote Sens. Environ.* **165**, 148–158 (2015).

17. Bontemps, N., Lacroix, P., Larose, E., Jara, J. & Taipe, E. Rain and small earthquakes maintain a slow-moving landslide in a persistent critical state. *Nat. Commun.* **11**, 780 (2020).

18. Booth, A. M. *et al.* Transient Reactivation of a Deep-Seated Landslide by Undrained Loading Captured With Repeat Airborne and Terrestrial Lidar. *Geophys. Res. Lett.* **45**, 4841–4850 (2018).

19. Schulz, W. H., Kean, J. W. & Wang, G. Landslide movement in southwest Colorado triggered by atmospheric tides. *Nat. Geosci.* **2**, 863–866 (2009).

20. Iverson, R. M. Landslide triggering by rain infiltration. *Water Resour. Res.* **36**, 1897–1910 (2000).

21. Petley, D. N., Carey, J. M., Ng, K.-Y., Massey, C. I. & Froude, M. J. Understanding patterns of movement for slow moving landslides. in *20th Symposium of the New Zealand Geotechnical Society* (eds. Alexander, G. & Chin, C.) 1–11 (New Zealand Geotechnical Society, 2017).

22. Dille, A. *et al.* When image correlation is needed: Unravelling the complex dynamics of a slow-moving landslide in the tropics with dense radar and optical time series. *Remote Sens. Environ.* **258**, 112402 (2021).

411 23. Lerner, D. N. Identifying and quantifying urban recharge: A review. *Hydrogeol. J.* **10**,
412 143–152 (2002).

413 24. Price, K. Effects of watershed topography, soils, land use, and climate on baseflow
414 hydrology in humid regions: A review. *Prog. Phys. Geogr.* **35**, 465–492 (2011).

415 25. Fletcher, T. D., Andrieu, H. & Hamel, P. Understanding, management and modelling of
416 urban hydrology and its consequences for receiving waters: A state of the art. *Adv.*
417 *Water Resour.* **51**, 261–279 (2013).

418 26. Michellier, C. Contribution to geo-risk prevention: population vulnerability
419 assessment in a data scarcity context. Case studies of Goma and Bukavu cities (DR
420 Congo). (in French). (Université Libre de Bruxelles - Vrije Universiteit Brussel, 2017).

421 27. Overbeek, F. Van & Tamás, P. A. Autochthony and insecure land tenure: the spatiality
422 of ethnicized hybridity in the periphery of post-conflict Bukavu, DRC. *J. East. African*
423 *Stud.* **12**, 290–309 (2018).

424 28. Hoffmann, K., Pouliot, M. & Muzalia, G. Constructed Anarchy: Governance, Conflict,
425 and Precarious Property Rights in Bukavu, Democratic Republic of the Congo. *Congo*
426 *Res. Briefs* **1**, 1–12 (2019).

427 29. Moeyersons, J. *et al.* A geomorphological assessment of landslide origin at Bukavu,
428 Democratic Republic of the Congo. *Eng. Geol.* **72**, 73–87 (2004).

429 30. Thomas, M. F. *Geomorphology in the tropics: a study of weathering and denudation in*
430 *low latitudes*. (John Wiley & Sons, 1994).

431 31. Dille, A. *et al.* Causes and triggers of deep-seated hillslope instability in the tropics –
432 Insights from a 60-year record of Ikoma landslide (DR Congo). *Geomorph.* **345**, 13
433 (2019).

434 32. Dewitte, O. *et al.* Constraining landslide timing in a data-scarce context: from recent
435 to very old processes in the tropical environment of the North Tanganyika-Kivu Rift
436 region. *Landslides* **18**, 161–177 (2021).

437 33. Jaboyedoff, M. *et al.* Human-Induced Landslides: Toward the analysis of
438 anthropogenic changes of the slope environment. in *Landslides and Engineered*

Slopes. Experience, Theory and Practice (eds. Avresa, S., Cascini, L., Picarelli, L. & Scavia, C.) **1**, 217–232 (CRC Press, 2016).

34. Depicker, A. *et al.* The added value of a regional landslide susceptibility assessment: The western branch of the East African Rift. *Geomorph.* **353**, 17 (2020).

35. Samsonov, S. & d'Oreye, N. Multidimensional time-series analysis of ground deformation from multiple InSAR data sets applied to Virunga Volcanic Province. *Geophys. J. Int.* **191**, 1095–1108 (2012).

36. Samsonov, S., Dille, A., Dewitte, O., Kervyn, F. & D'Oreye, N. Satellite interferometry for mapping surface deformation time series in one, two and three dimensions: a new method illustrated on a slow-moving landslide. *Eng. Geol.* **266**, (2020).

37. Nobile, A. *et al.* Multi-Temporal DInSAR to Characterise Landslide Ground Deformations in a Tropical Urban Environment: Focus on Bukavu (DR Congo). *Remote Sens.* **10**, 626 (2018).

38. Balegamire, C. *et al.* Vulnerability of buildings exposed to landslides : a spatio-temporal assessment in Bukavu (DR Congo). *Geo. Eco. Trop.* **41**, 263–278 (2017).

39. Krzeminska, D. M., Bogaard, T. A., Malet, J. P. & Van Beek, L. P. H. A model of hydrological and mechanical feedbacks of preferential fissure flow in a slow-moving landslide. *Hydrol. Earth Syst. Sci.* **17**, 947–959 (2013).

40. Schulz, W. H. *et al.* Landslide kinematics and their potential controls from hourly to decadal timescales: Insights from integrating ground-based InSAR measurements with structural maps and long-term monitoring data. *Geomorph.* **285**, 121–136 (2017).

41. Van Asch, T. W. J., Buma, J. & Van Beek, L. P. H. A view on some hydrological triggering systems in landslides. *Geomorph.* **30**, 25–32 (1999).

42. Schulz, W. H., McKenna, J. P., Kibler, J. D. & Biavati, G. Relations between hydrology and velocity of a continuously moving landslide-evidence of pore-pressure feedback regulating landslide motion? *Landslides* **6**, 181–190 (2009).

43. Nereson, A. L., Davila Olivera, S. & Finnegan, N. J. Field and Remote-Sensing Evidence

for Hydro-mechanical Isolation of a Long-Lived Earthflow in Central California. *Geophys. Res. Lett.* **45**, 9672–9680 (2018).

44. Malet, J.-P., Maquaire, O. & Calais, E. The use of global positioning system techniques for the continuous monitoring of landslides: Application to the Super-Sauze earthflow (Alpes-de-Haute-Provence, France). *Geomorph.* **43**, 33–54 (2002).

45. Massey, C. I., Petley, D. N. & McSaveney, M. J. Patterns of movement in reactivated landslides. *Eng. Geol.* **159**, 1–19 (2013).

46. Corominas, J., Moya, J., Ledesma, A., Lloret, A. & Gili, J. A. Prediction of ground displacements and velocities from groundwater level changes at the Vallcebre landslide (Eastern Pyrenees, Spain). *Landslides* **2**, 83–96 (2005).

47. Sidle, R. C. & Bogaard, T. A. Dynamic earth system and ecological controls of rainfall-initiated landslides. *Earth-Science Rev.* **159**, 275–291 (2016).

48. Sidle, R. C. & Ochiai, H. *Landslides : processes, prediction, and land use*. *Water resoures monograph* (American Geophysical Union, 2006).

49. Ollier, C., Calcaterra, D. & Parise, M. Studies in weathering and slope movements-an introduction. *Geomorph.* **87**, 101–103 (2007).

50. Fan, X. *et al.* Earthquake-induced chains of geologic hazards: patterns, mechanisms, and impacts. *Rev. Geophys.* **57**, 421–503 (2019).

51. Bogaard, T. A. & Greco, R. Landslide hydrology: from hydrology to pore pressure. *Wiley Interdiscip. Rev. Water* **3**, 439–459 (2016).

52. Holcombe, E. A., Beesley, M. E. W., Vardanega, P. J. & Sorbie, R. Urbanisation and landslides: Hazard drivers and better practices. *Proc. Inst. Civ. Eng. Civ. Eng.* **169**, 137–144 (2016).

53. Omondi, P. A. o. *et al.* Changes in temperature and precipitation extremes over the Greater Horn of Africa region from 1961 to 2010. *Int. J. Climatol.* **34**, 1262–1277 (2014).

54. Souverijns, N., Thiery, W., Demuzere, M. & Lipzig, N. P. M. V. Drivers of future changes in East African precipitation. *Environ. Res. Lett.* **11**, (2016).

55. Masson-Delmotte, V. *et al. Contribution of Working Group I to the Sixth Assessment Report of the Intergovernmental Panel on Climate Change.* (2021).

56. Agliardi, F., Scuderi, M. M., Fusi, N. & Collettini, C. Slow-to-fast transition of giant creeping rockslides modulated by undrained loading in basal shear zones. *Nat. Commun.* **11**, 1–11 (2020).

57. Satterthwaite, D., Huq, S., Pelling, M., And, H. R. & Lankao, P. R. Adapting to Climate Change in Urban Areas : The Possibilities and Constraints in low- and middle-income nations. *Int. Inst. Environ. Dev.* 1–112 (2007).

58. Anderson, M. G. & Holcombe, E. *Community-Based Landslide Risk Reduction*. (The World Bank, 2013).

Methods

High temporal resolution landslide motion using InSAR. We performed interferometric processing of Synthetic Aperture Radar (InSAR) images acquired by the COSMO-SkyMed (CSK) and Sentinel-1 SAR sensors over 4.5 years (March 2015 - August 2019). We generated 2,575 interferograms from 363 CSK and 227 Sentinel-1 images in both ascending and descending geometries using the MasTer Engine processing chain[59–61]. We used a multilooking factor of 5 in azimuth and range for CSK and 1 in azimuth and 7 in range for Sentinel-1 to obtain a final squared pixel size of ~15 m. Interferograms were processed with temporal baselines ranging from 2 to 80 days. A minimum coherence threshold (>0.4) was defined to avoid unnecessary processing in vegetated zones where the overall coherence is not sufficient to provide satisfactory deformation maps. The topographic phase was removed using the recent ALOS 3D DEM[62]. We processed the resulting interferograms using the Multidimensional Small Baseline Subset[35,36] (MSBAS) processing chain. By combining interferograms from different SAR datasets (i.e., sensors and orbits), MSBAS provides 2D (east-west and vertical) or 3D (assuming the slide motion is parallel to the surface) displacements estimates with a combined temporal resolution[35,36]. Integrating ascending and descending CSK and Sentinel-1 images, the average number of days between two deformation measurements is down to 2.8 days, with a maximum of 19 days. We used measurements from dGNSS surveys campaigns over 20 benchmarks for validating InSAR velocities[36,37].

Measuring rapid landslide motion. Given that displacement rates of the fastest landslide unit are above intrinsic measurement limits of conventional InSAR[22,36,37], we additionally measured landslide motion using automated pixel tracking applied on optical images. We conducted our analysis on three precisely orthorectified stereo and triplet Pléiades satellite images spanning a 5.5-year period (March 2013, July 2013, July 2018). Photogrammetric processing of Pléiades images (bundle adjustment, topographic surface reconstruction and orthorectification) was performed in MicMac[63], assisted with 27 ground control points (GCPs) located via dGNSS between 2014 and 2018 in the city of Bukavu and its surroundings. Alongside satellite orthomosaics, two very-high resolution DSMs and orthomosaics were created from images acquired from applying Structure-from-Motion photogrammetry to Unoccupied Aircraft System photos (UAS-SfM[64]) of Funu landslide from Sep.-Oct. 2017 and Oct. 2018. Flight paths, flight speed and altitude to ground were pre-programmed in order to avoid/minimize motion blur and maintain a uniform ~8.2 cm/pixel Ground Sampling Distance all along the survey area (Supplementary Table 2). Areas of 4.5 km² (2017) and 3.5 km² (2018) were surveyed over the 1.5 km² size of the landslide, ensuring the presence of stable locations within the output models. In addition to Nadir views (1,750 and 490 images for 2017 and 2018, respectively), sets of 400 and 280 oblique (15-20°) images were acquired, aiming at reducing systematic DSM errors, (e.g., [65]). UAS photogrammetric workflow was performed in Metashape Pro[66]. We used a co-alignment workflow to reduce registration errors between epochs[22,67]. COSI CORR software package[68] was used to perform automated pixel tracking on the 0.5 m resolution Pléiades and the 0.08 m resolution UAS-SfM orthomosaics. We used decreasing windows sizes (from 512 to 32 pixels) and 16 pixels steps to measure the east–west (EW) and north–south (NS) components of the surface displacement from the orthomosaics.

Morphological landslide units. Most large landslides are composed of several internal units which may move semi-independently one to another. These units report evidence of internal deformation processes, and their zonation therefore help understand the behaviour of different parts of the landslide[69,70]. We used the newly built very-high resolution UAS-SfM DSM to identify individual internal landslide units based on an analysis of the landslide surface topography[69,70] (Extended Data Fig 4.).

Estimating surface strain and landslide depth. Using horizontal measurements of surface motion, we estimated landslide depth and surface strain. Strain rates were measured by combining horizontal mean velocity fields from SAR interferometry (2015-2019) and automated pixel tracking for the units with fastest movements (2013-2018). Given the high spatial resolution (15x15 m pixels), strain rate tensor measurements are very sensitive to noise. Therefore we used a plane-strain mass continuity equation considering a range of deformation pixels and neglecting the vertical component of motion[15]. No in-situ data (e.g., from geophysical measurements) are available, but proxies such as the escarpment depth (50-100m) and the morphological study of landslide unit allowed for rough estimations of the landslide thickness[71].

Time series and pore pressure analysis. We extracted InSAR displacement time series over 24 sites within the landslide (Extended Data Fig. 5) to constrain velocity patterns of the individual landslide units over the four seasonal cycles (period 2015-2019). 2D InSAR (east-west and up-down) was here chosen over 3D solution for being presumably more robust for the detailed study of kinematics. Also, neglecting north-south component of motion has little influence considering its much lower magnitude[35]. Given the rates of deformation of the fastest landslide unit (up to 3 m yr^{-1}, i.e., a value which cannot be measured with conventional InSAR technique[22]; Fig. 2d), we analysed only time series of displacement extracted close to its borders, where surface velocities are of lower magnitude. To highlight the overall pattern of motion and improve signal-to-noise ratio, we smoothed the velocity time series using a lowess filter (locally weighted linear regression) with a window size of ~90 days. While more robust than moving average, this smoothing may introduce a temporal shift to the acceleration patterns. We estimated uncertainties for each site from the standard deviation of the displacement measured over the four neighbouring pixels[72]. Times series for the 24 sites were sorted in three groups based on similitude in their kinematic behaviour, i.e., the central units (13 sites), fastest unit (eight sites) and active toe (three sites); see Extended Data Figs. 5 and 7 and Supplementary Discussion. We compared changes in landslide motion to earthquake catalogues and rainfall-induced changes in pore-water pressure, that in absence of in-situ measurements were simulated through a homogenous 1D diffusion model[13,15]. We selected earthquake events significant enough for the potential triggering of hillslope instability over Funu based on the Keefer's[73] relationship between maximum epicentral

distances to landslides and earthquake magnitude. It includes seven earthquakes with a magnitude (Mw) between 4.7 and 5.9 and an epicentral distance ranging from 21 to 52 km[74–76] (Extended Data Fig. 1b). Precipitation data consists of rain-gauge measurements acquired ~2 km from the landslide for the period October 2016 – April 2019 as well as version 6 of the Integrated Multi-satellite Retrievals for Global Precipitation Measurement (IMERG-GPM v6 Final[77]) for the period 2000 – 2019 and validated for the region[78]. Note that IMERG-GPM data generally underestimate actual rainfall amounts[78]. Precipitation data fed a simple 1D diffusion model of pore-water pressure changes[13,15]. The pore pressure model was run to steady state by adding 15 years of IMERG-GPM precipitation data (2000 - 2015) before the period of the present study (Extended Data Fig. 11). We solved for best fit the value for landslide diffusivity by minimizing the Root Mean Square Error (RMSE) misfit between normalised simulated pore-water pressure and normalised average velocity time series over the landslide. For a landslide thickness of 30 m, a best fit soil diffusivity of 1.0×10^{-4} m^2/s generally provided good agreement between measured velocity and simulated pore-water pressure changes. This value is relatively high but falls in the range measured e.g. for landslides in weathered basalts[79]. Considering the absence of in-situ measurements and the simple approach applied, we used this pore-water pressure solution for the entire landslide. Limits of this approach are e.g., described in ref[13,15]. Also, since our aim is exploring timing and changes in relative strength of the pore-pressure over time, only normalised velocity and pore-pressure values are compared. Value for each were normalized to range between minimum (min = 0) and maximum (max = 1).

Multi-decadal analysis of urban growth and slope instability. We combined historical panchromatic, ~1/50,000 scale, aerial photographs available at the Royal Museum for Central Africa (Belgium) and optical satellite images to measure landslide motion and document urban growth between 1947 and 2018 (Fig. 5, Extended Data Fig. 9). 1947 images originate from a scanned mosaic georeferenced using 35 GCPs located on stable ground. Orthomosaics for 1959 and 1974 were made by applying recent Multiview Stereo Photogrammetry (MVS) approaches[80] on aerial photos in Metashape Pro[66]. We used 45 and 30 GCPs for georeferencing, respectively. GCPs locations were extracted from the 1-meter resolution DSM and orthomosaic obtained from the July 2013 Pléiades stereo pair. The same DSM was used to orthorectify the 1959 and 1974 orthomosaic and a 2001 Ikonos satellite image. With

additions from the 2013 and 2018 Pléiades and the 2017-2018 UAS-SfM orthomosaics, we collected images providing six windows in time to gather information on the landslide over the last 70 years.

Drastic changes in urban fabric since 1947 (see Extended Data Figs. 9, 10) and differences in origin, quality and resolution of the images hampered the use of automated pixel tracking algorithms to evaluate changes in surface velocity[81]. We therefore manually tracked the location of identifiable benchmarks present in all images between 1959 and 2018 and distributed over the landslide to measure displacements over the years. 48 benchmarks are used, representing building corners, road crossings, etc. 11 benchmarks are located outside the landslide and 37 inside (including 8 within the fastest landslide unit and 6 within the most active sections of the landslide toe). Urbanisation being limited to the toe of the landslide in 1947, surface velocities could not be estimated for the period 1947-1959. Errors in location (related to picking accuracy and orthorectification errors) are estimated to ± 0.2–4.0 m. We estimated the level of background noise (e.g., associated with picking errors, differences in image origin and potential inaccurate orthorectifications) from the velocity measured in the 11, presumably stable sites located outside the landslide. It varies from 0.09 to 0.18 m yr^{-1} depending on the image pairs (Fig. 5). We also manually mapped urban fabric (defined as zones with a dominance of build-up and impervious surfaces) on each image to investigate changes in proportion of built-up area within the landslide over time. We used the three same categories (i.e., central units, fastest unit and active toe) as for the kinematic analysis. Note that the rates of displacement and the size of the fastest moving unit prevented the use of medium resolution satellite images (e.g. Landsat and SPOT) to study their motion.

Slope and man-made drainage systems. We modelled the slope drainage using the Rho 8 method[82] applied on the UAS DSM (October 2017; Fig. 4a). We updated the localisation and condition of the storm and sewage drains (Fig. 4b) mapped for this zone of Bukavu in 2003[83] and 2017[84] combining data collected in the field and visual observations of the 0.08 m resolution UAS orthomosaics (Fig. 4cde).

Data Availability:

Data used in this study are available for download from 10.5281/zenodo.7118267. The satellite imagery that supports the findings of this study is available from the space agencies and satellite operators (ESA/Copernicus, ASI, CNES/Airbus) but restrictions apply to the availability of some of these data, which were used under license for the current study, and so are not systematically available publicly. Sentinel data are made available by ESA, https://scihub.copernicus.eu/.

Code Availability:

All computer codes used in this work are available from the authors upon reasonable request.

Extended Data Figures

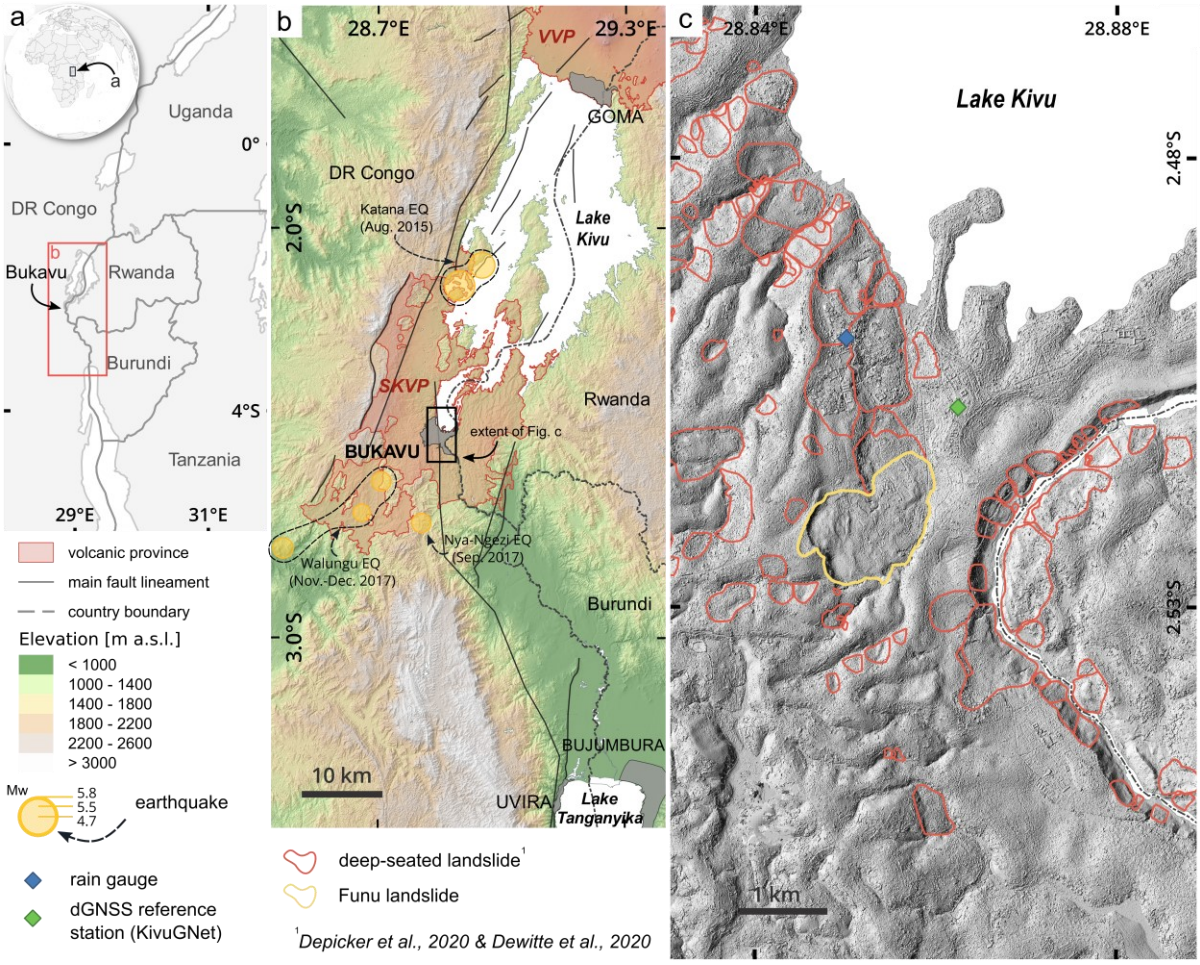

Extended Data Fig. 1. | Regional context and overview of the city of Bukavu. a, Location of Bukavu, DR Congo. **b**, The Kivu Rift, showing main fault lineaments, the South Kivu Volcanic Province (SKVP) and the location of the main earthquakes that occurred during the

period 2015-2019. **c**, Outlines of Funu landslide (in yellow) and other deep-seated landslides[10,11] (in red) mapped in the area. Background digital elevation model is obtained from photogrammetric processing of stereo Pléiades images from July 2013 (see Methods).

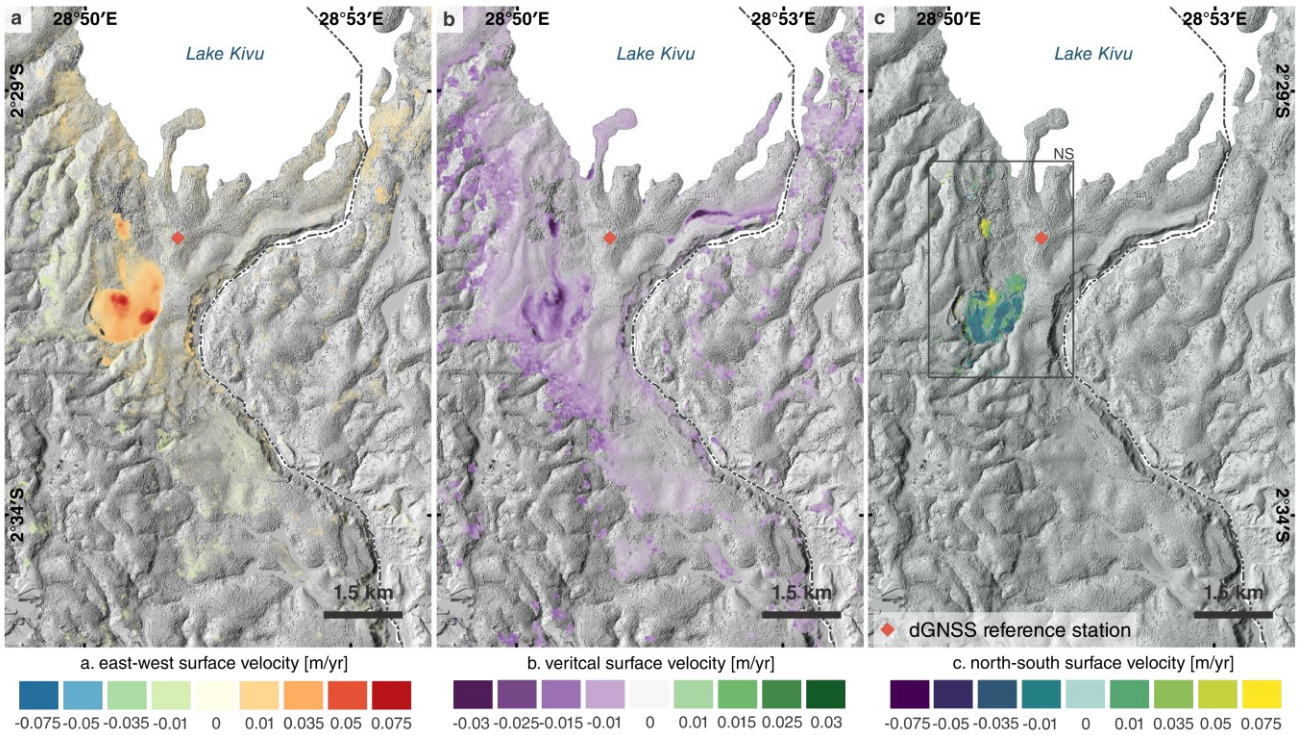

Extended Data Fig. 2. | Surface deformation maps over the city of Bukavu. a, East-west, **b**, vertical and **c**, north-south surface velocities measured from combined interferometric processing of CSK and Sentinel 1 images. Background digital elevation model is obtained from photogrammetric processing of stereo Pléiades images from July 2013 (see Methods).

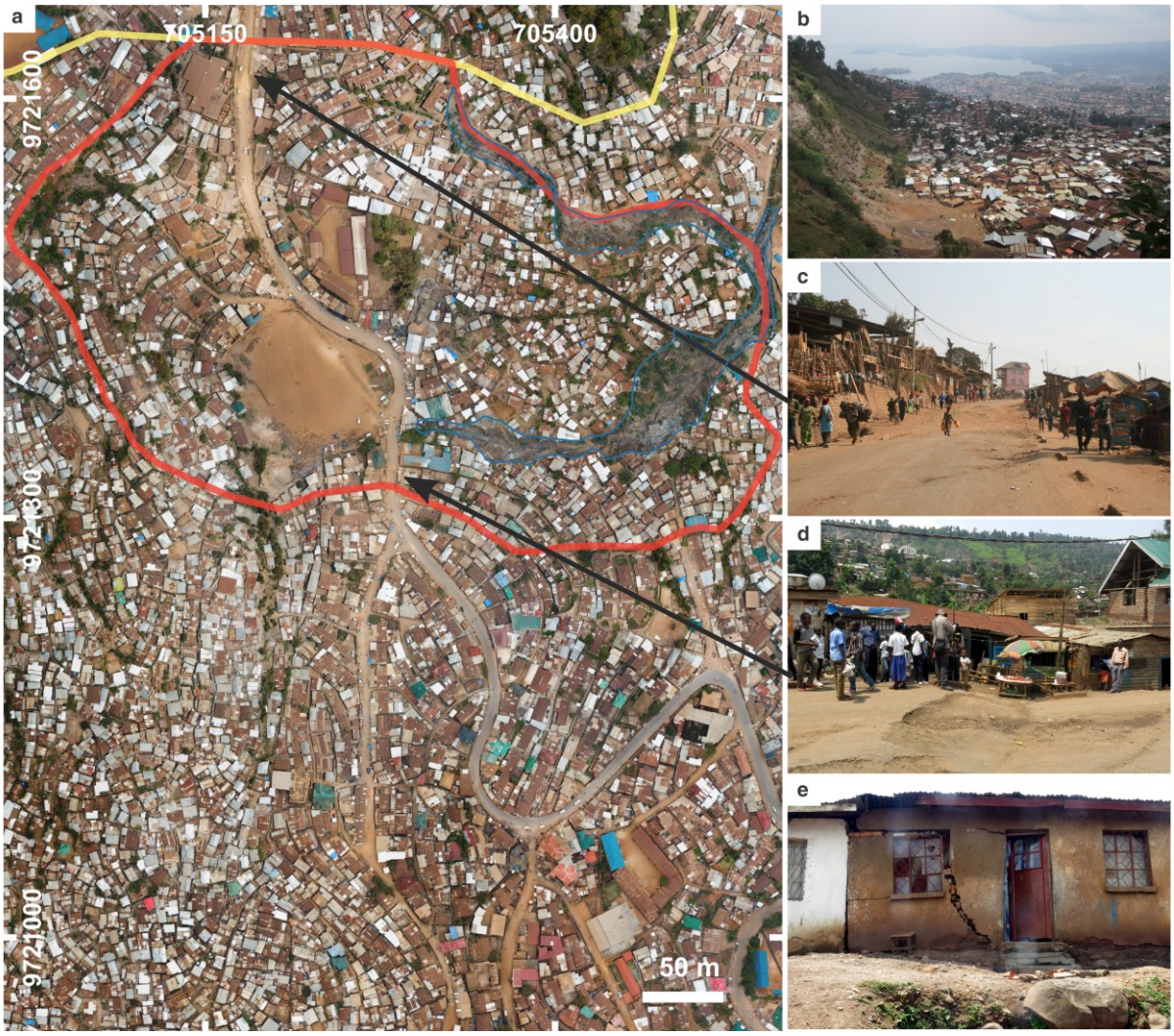

Extended Data Fig. 3 | Urban density and landslide impacts. a, Very-high resolution UAS-SfM orthomosaic (Oct. 2018) of a section the landslide that includes the 14-ha 'fastest unit' (in red). Note the very-high density of individual building (the landslide population is estimated to ~55 000 inhab./km²; [4]). In blue is highlighted the size of the two gullies that partially delimit the toe of the fastest unit. **b**, View of the landslide taken from the headscarp. Lake Kivu is visible in the background. **c**, and **d**, damages to a road at the border of the fastest unit, where velocity gradients are the highest. **e**, damages to a house within the landslide. Extent of **a**, is shown in Extended Data Fig. 4.

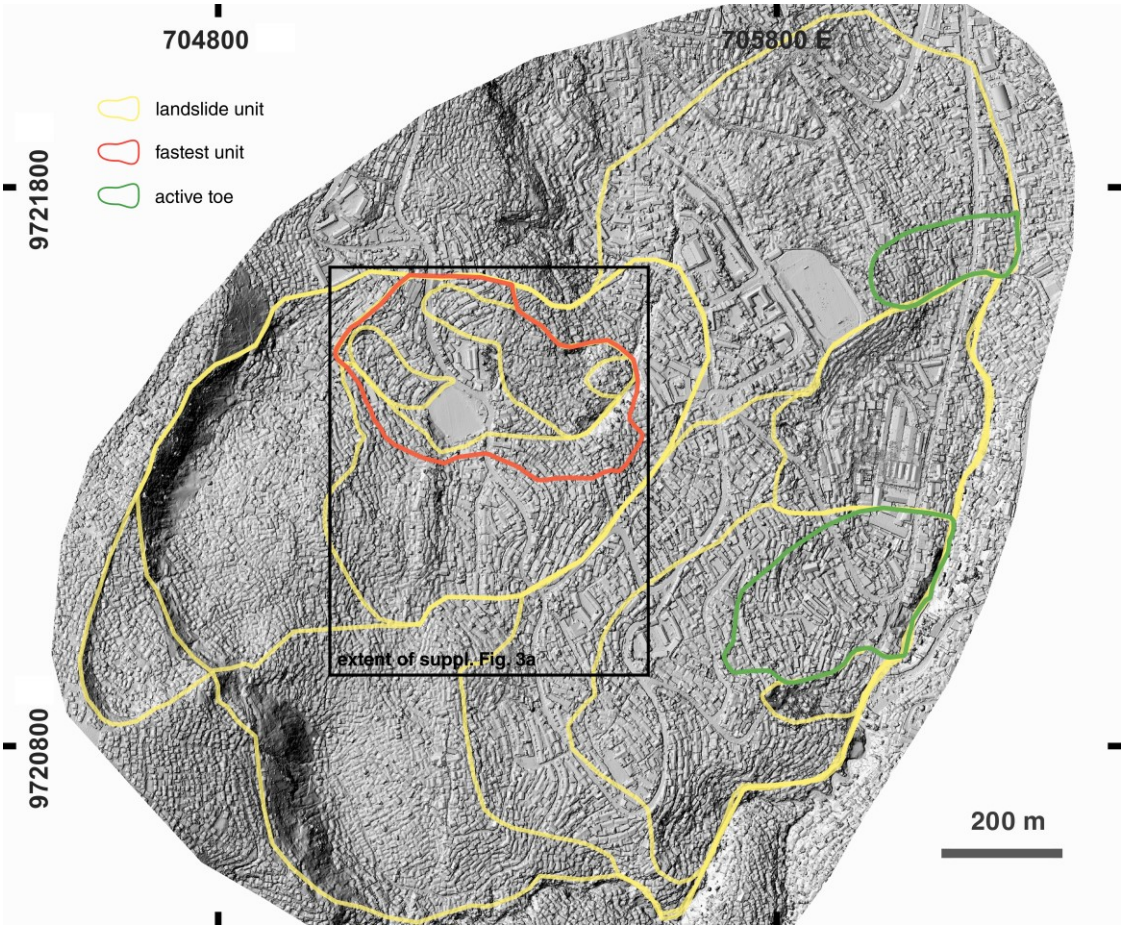

Extended Data Fig. 4. | Morphological landslide units. Very-high resolution shaded relief of the landslide obtained from UAS-SfM (Oct. 2017) on which are outlined the different landslide morphologic units. In green and red are shown the 'fastest unit' and the 'active toe' units, grouped based on their kinematic behaviour. Note the dense urban fabric.

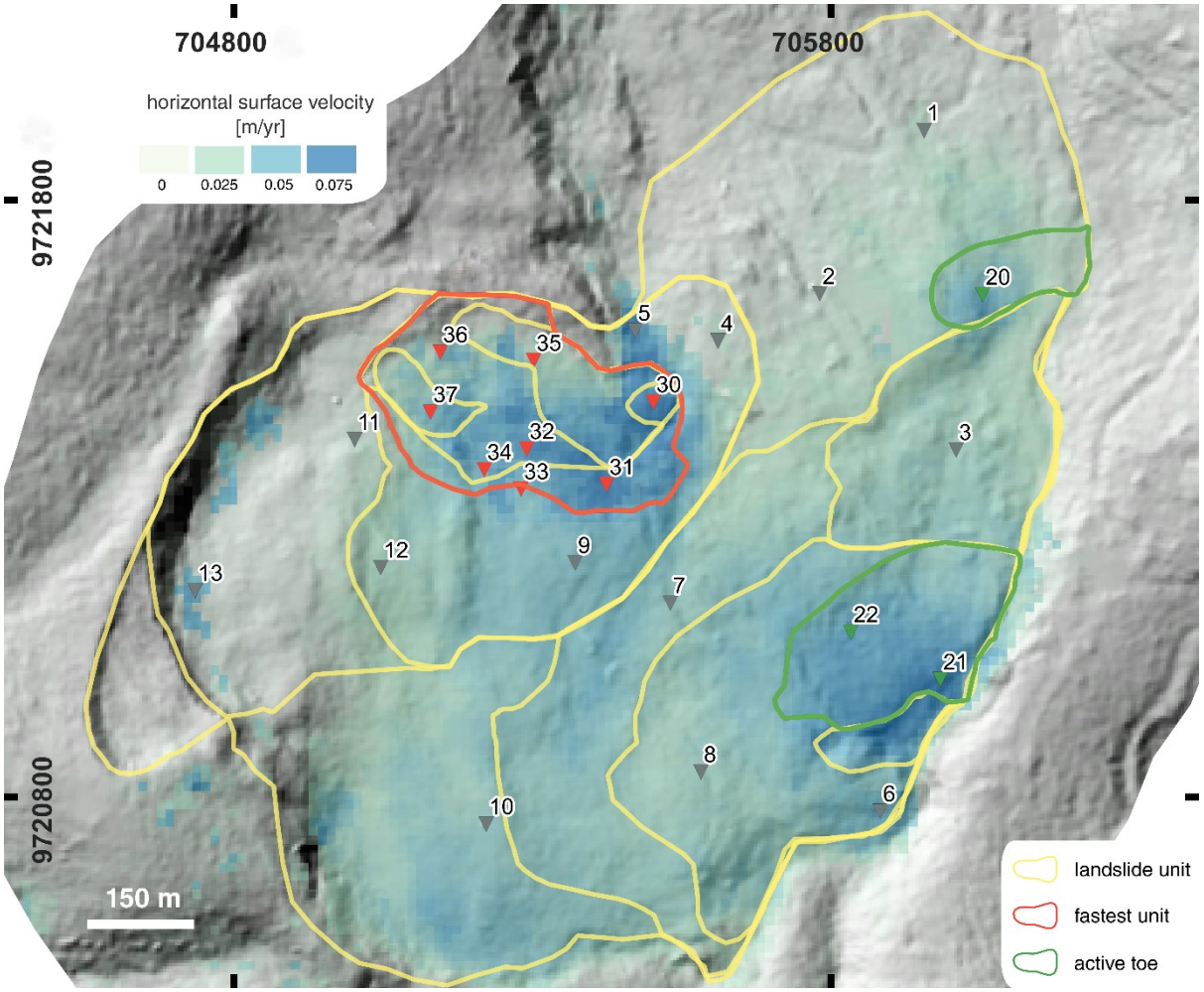

Extended Data Fig. 5. | Sites of displacement time series. Location of the sites where InSAR displacement time series were extracted. In red are shown sites located in and grouped as 'fastest unit' (8 sites), in green the 'active toe' (3 sites) and in grey the 'central units' (13 sites).

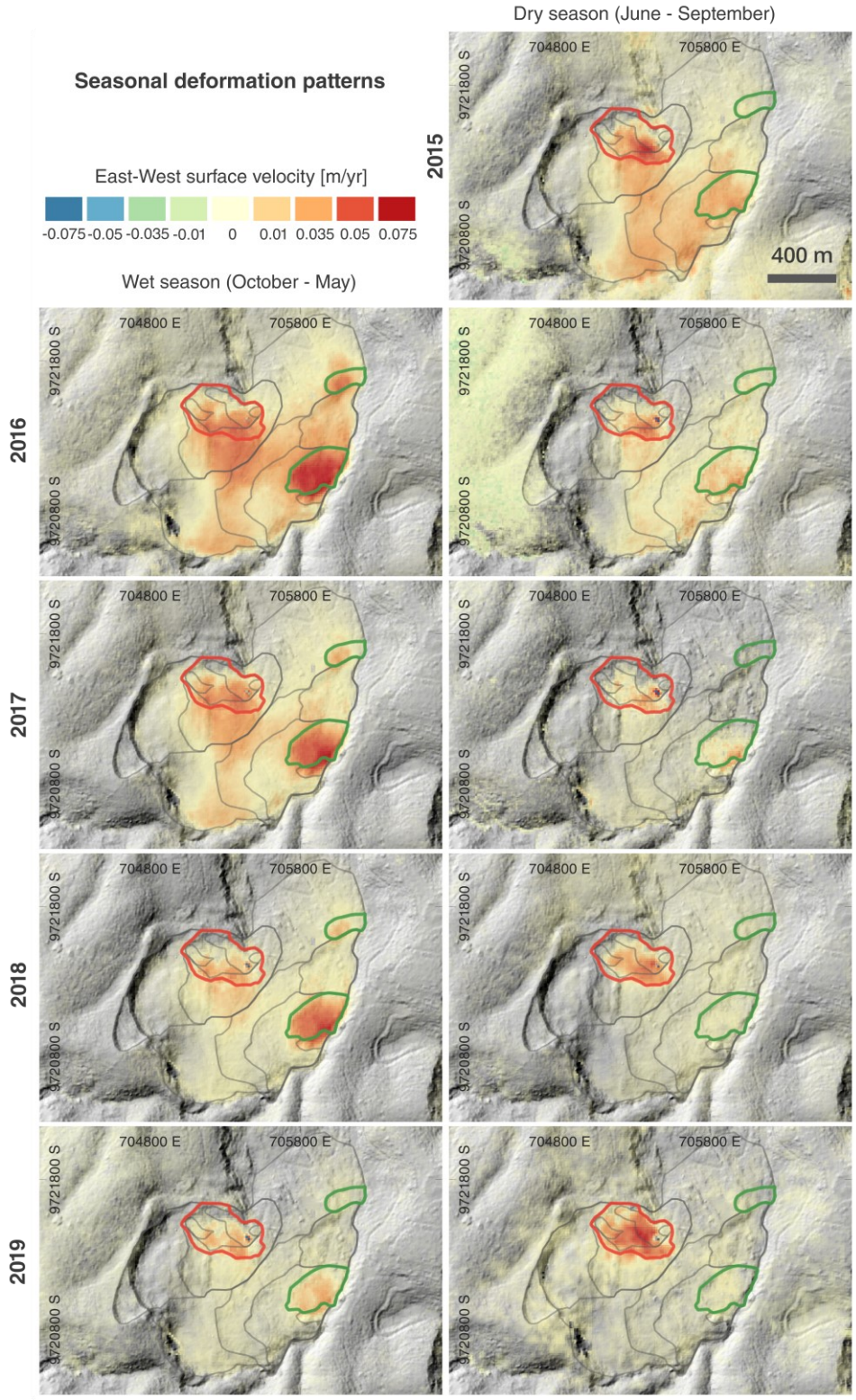

Extended Data Fig. 6. | Seasonal deformation pattern. East-west surface velocities are measured by InSAR for each season (defined as dry from June to September and wet from October to May). The 'fastest unit' is outlined in red and the 'active toe' in green.

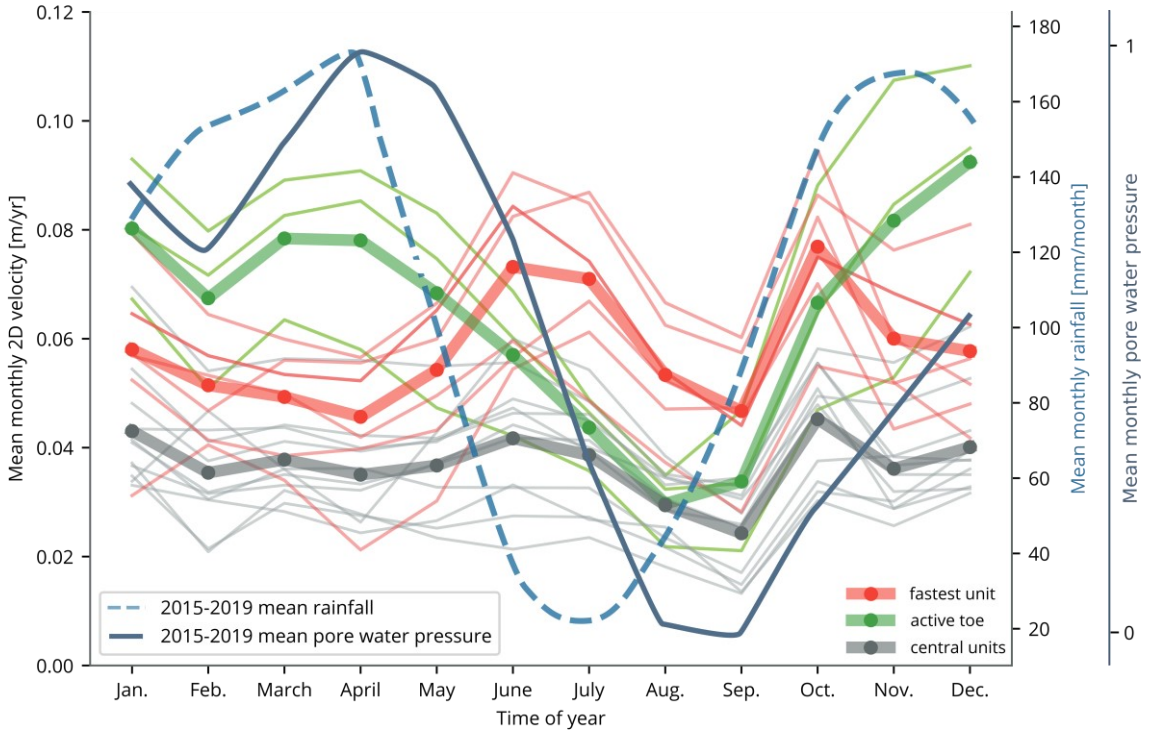

716

717 **Extended Data Fig. 7. | Monthly landslide velocities.** 2D InSAR velocities (east-west and
718 vertical) averaged by months for the period 2015-2019. Thick lines represent mean 2D velocity
719 time series from all sites in landslide 'active toe', 'fastest unit' and the landslide 'central units'
720 (see Extended Data Fig. 5 for sites locations). The 2015-2019 mean monthly rainfall and pore
721 water pressure in the slope are displayed. A detailed analysis of the different seasonal velocity
722 patterns for the different landslide units is provided as supplementary discussion (1.1).

723

724

725

726

727

728

729

730

731

732

733

734

735

736

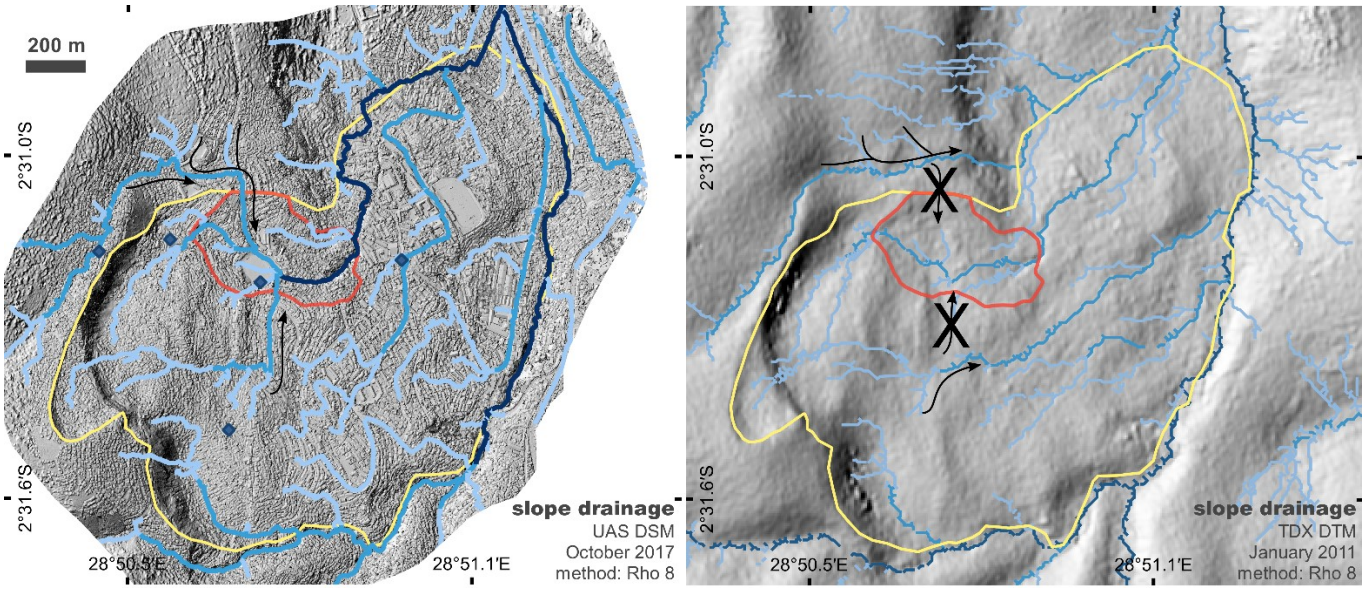

Extended Data Fig. 8. | Simulations of slope surface drainage. a, Slope surface drainage over Funu landslide simulated on very-high-resolution UAS-SfM DSM. Arrows highlight zones outside the natural catchment of the 'fastest unit' (in red) from which water is conveyed by man-made infrastructure. Blue diamonds show the location of springs. **b,** Slope surface drainage simulated on a Digital Terrain Model (where the influence of manmade infrastructure is assumed negligeable).

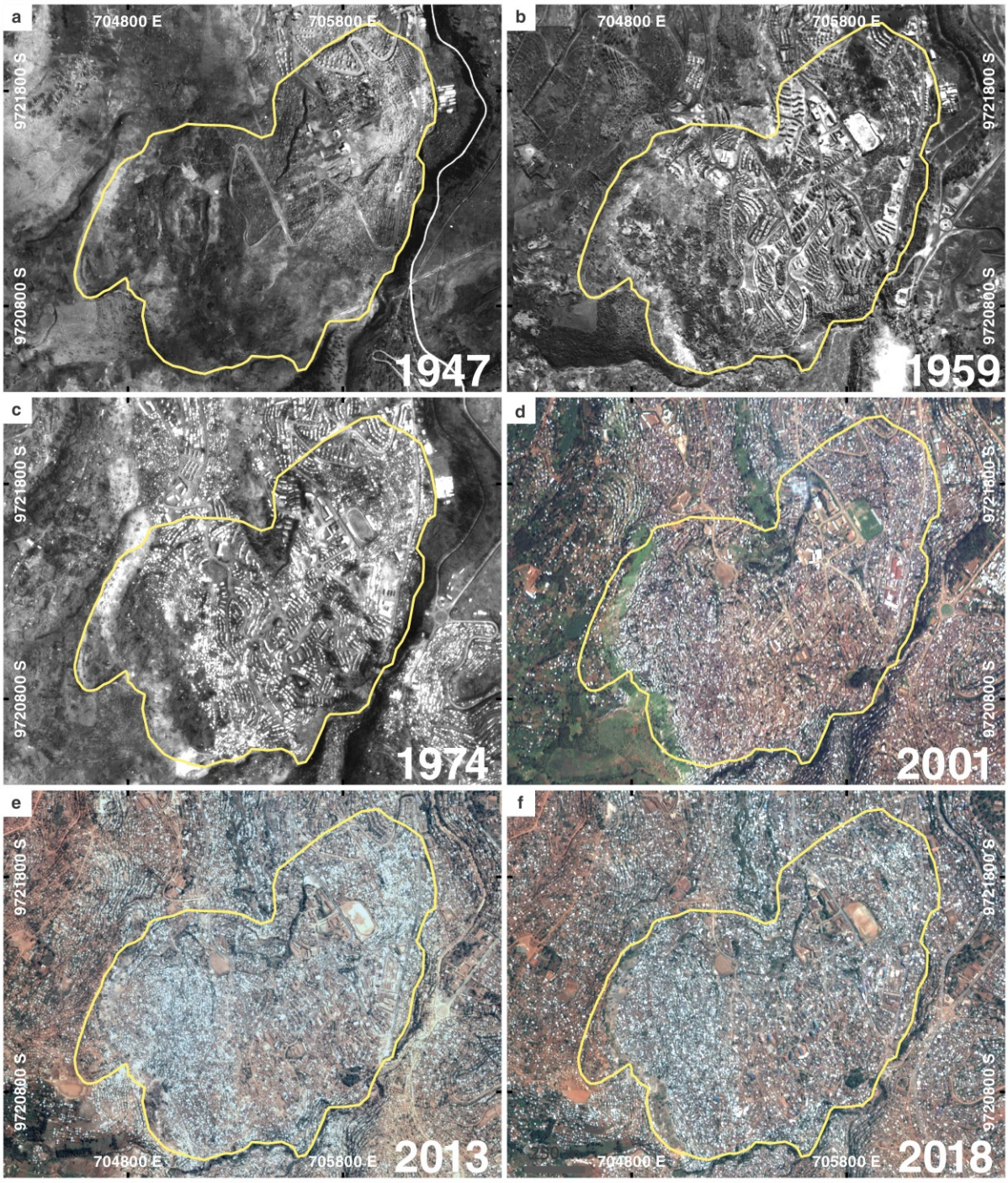

Extended Data Fig. 9. | Progressive urbanisation of Funu landslide. Aerial and satellite images of Funu landslide for the period 1947 until 2018. 1947, 1959 and 1974 are derived from historical aerial images available at the Royal Museum for Central Africa (Belgium). 2001 is an Ikonos satellite orthomosaic and 2013 and 2018 are very-high resolution Pléiades orthomosaics. These images were used in the evaluation of the changes in landslide motion and urban fabric over the last 70 years (Fig. 4).

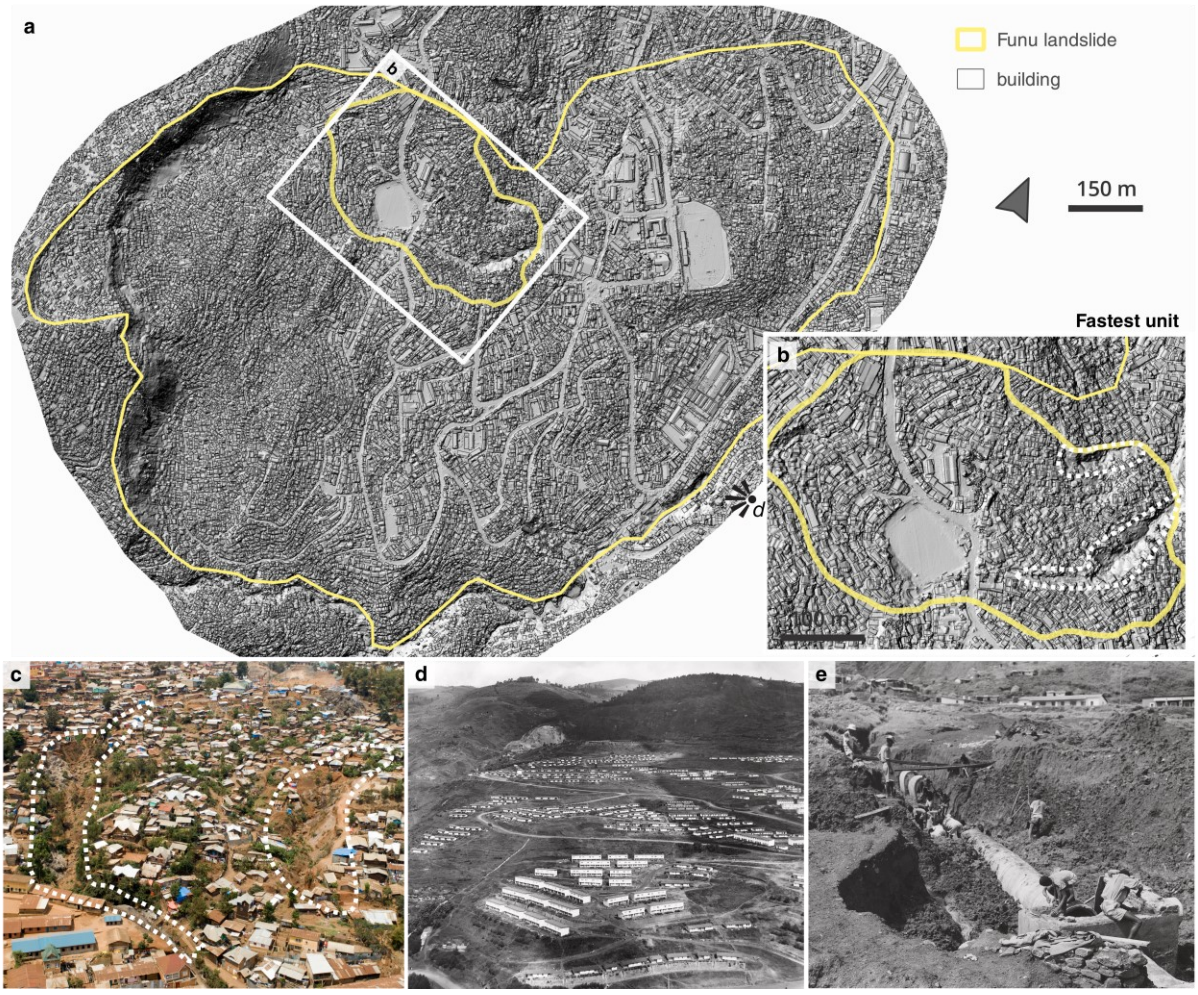

Extended Data Fig. 10. | Urban development at Funu landslide. a, Very-high resolution shaded relief of the landslide from UAS-SfM (Oct. 2017). The resolution stresses the very-high density of individual building (the population is estimated to ~55 000 inhab./km²; [4]). **b,** Funu landslide fastest unit, where characteristic landslide features (such as surface discontinuities, tension cracks, marked steps in slope profile) translating important internal deformation are the most visible. Two gullies (also shown in **c,**) delimit a sub-unit where velocities are the highest (up to 3 m/yr). **d,** Historical picture showing part of Funu landslide in 1959. It highlights the low housing density at that time. **e,** Illustrates work on the drainage systems in Bukavu (photo taken in 1959).

Methods-only references:

59. Derauw, D. Phasimétrie par Radar à Synthèse d'Ouverture; théorie et applications.

(Université de Liège, 1999).

60. d'Oreye, N., Derauw, D., Samsonov, S., Jaspard, M. & Smittarello, D., MasTer: A Full Automatic Multi-Satellite InSAR Mass Processing Tool for Rapid Incremental 2D Ground Deformation Time Series. *Int. Geosci. Remote Sens. Symp.,* 1899-1902 (2021).

61. Derauw, D., d'Oreye, N., Jaspard, M., Caselli, A. & Samsonov, S. Ongoing automated ground deformation monitoring of Domuyo - Laguna del Maule area (Argentina) using Sentinel-1 MSBAS time series: Methodology description and first observations for the period 2015–2020. *J. South Am. Earth Sci.* **104**, 102850 (2020).

62. Tadono, T. *et al.* Generation of the 30 m-mesh global digital surface model by ALOS PRISM. *Int. Arch. Photogramm. Remote Sens. Spat. Inf. Sci.* **XLI**, 157–162 (2016).

63. Rupnik, E., Daakir, M. & Pierrot-Deseilligny, M. MicMac – a free, open-source solution for photogrammetry. *Open Geospatial Data, Softw. Stand.* **2**, 14 (2017).

64. Eltner, A. *et al.* Image-based surface reconstruction in geomorphometry-merits, limits and developments. *Earth Surf. Dyn.* **4**, 359–389 (2016).

65. James, M. R. & Robson, S. Mitigating systematic error in topographic models derived from UAV and ground-based image networks. *Earth Surf. Process. Landforms* **39**, 1413–1420 (2014).

66. Agisoft. Agisoft Metashape Pro. (2020).

67. Cook, K. L. & Dietze, M. Short Communication: A simple workflow for robust low-cost UAV-derived change detection without ground control points. *Earth Surf. Dyn.* **7**, 1009–1017 (2019).

68. Leprince, S., Ayoub, F., Klinger, Y. & Avouac, J. P. Co-Registration of Optically Sensed Images and Correlation (COSI-Corr): An operational methodology for ground deformation measurements. *Int. Geosci. Remote Sens. Symp.* 1943–1946 (2007).

69. Fleming, R. W., Baum, R. L. & Giardino, M. *Map and Description of the Active Part of the Slumgullion Landslide, Hinsdale County, Colorado*. (1999).

70. Parise, M. Observation of surface features on an active landslide, and implications for understanding its history of movement. *Nat. Hazards Earth Syst. Sci.* **3**, 569–580

(2003).

71. Dewitte, O. & Demoulin, a. Morphometry and kinematics of landslides inferred from precise DTMs in West Belgium. *Nat. Hazards Earth Syst. Sci.* **5**, 259–265 (2005).

72. Samsonov, S. & D'Oreye, N. Multidimensional Small Baseline Subset (MSBAS) for Two-Dimensional Deformation Analysis: Case Study Mexico City. *Can. J. Remote Sens.* **43**, 318–329 (2017).

73. Keefer, D. K. Investigating landslides caused by earthquakes - A historical review. *Surv. Geophys.* **23**, 473–510 (2002).

74. Delvaux, D. *et al.* Seismic hazard assessment of the Kivu rift segment based on a new seismotectonic zonation model (western branch, East African Rift system). *J. African Earth Sci.* **134**, 831–855 (2017).

75. Oth, A. *et al.* KivuSNet: The First Dense Broadband Seismic Network for the Kivu Rift Region (Western Branch of East African Rift). *Seismol. Res. Lett.* **88**, 49–60 (2017).

76. USGS. USGS Earthquake Hazards Program. (2020). Available at: https://earthquake.usgs.gov/.

77. Huffman, G., Bolvin, D., Braithwaite, D., Hsu, K. & Joyce, R. *NASA Global Precipitation Measurement - Integrated Multi-satellite Retrievals for GPM*. *Algorithm Theoretical Basis Document v06* (2019).

78. Monsieurs, E. The potential of satellite rainfall estimates in solving regional landslide hazard modelling in data-scarce contexts. (Royal Museum for Central Africa / Université de Liège, 2020).

79. Baum, R. L., Messerich, J. & Fleming, R. W. Surface deformation as a guide to kinematics and three-dimensional shape of slow-moving, clay-rich landslides, Honolulu, Hawaii. *Environ. Eng. Geosci.* **4**, 283–306 (1998).

80. Bakker, M. & Lane, S. N. Archival photogrammetric analysis of river–floodplain systems using Structure from Motion (SfM) methods. *Earth Surf. Process. Landforms* **42**, 1274–1286 (2017).

81. Dewitte, O. *et al.* Tracking landslide displacements by multi-temporal DTMs: A

combined aerial stereophotogrammetric and LIDAR approach in western Belgium. *Eng. Geol.* **99**, 11–22 (2008).

82. Fairfield, J. & Leymarie, P. Drainage networks from grid digital elevation models. *Water Resour. Res.* **27**, 709–717 (1991).

83. Trefois, P. *et al. Géologie urbaine de Bukavu: interaction entre la stabilité du sol et la pression démographique*. (2003).

84. Kalikone Buzera, C. *et al.* Ground deformation impact on the vulnerability of water and electricity distribution networks in Bukavu (DR Congo). *Geo. Eco. Trop.* **41**, 279–292 (2017).